Supporting Information

Improved electrochemical performance of $FeO_x(OH)$/IF electrode via *in-situ* surface modification with organic naphthoquinone molecules

Zongyi Shang,[†] *Jiayu Li,*[†] *Yu Chen,*[†] *Zhigang Zhao,*[*,‡] *and Caixia Zhou*[*,†]

[†] Key Laboratory of Pollution Control Chemistry and Environmental Functional Materials for Qinghai-Tibet Plateau of the National Ethnic Affairs Commission, School of Chemistry and Environment, Southwest Minzu University, Chengdu 610041, China

[‡] Key Laboratory of General Chemistry of the National Ethnic Affairs Commission, School of Chemistry and Environment, Southwest Minzu University, Chengdu 610041, China

Corresponding author:
C.X. Zhou: cx_Zhou123@163.com
Z.G. Zhao: zzg63129@163.com

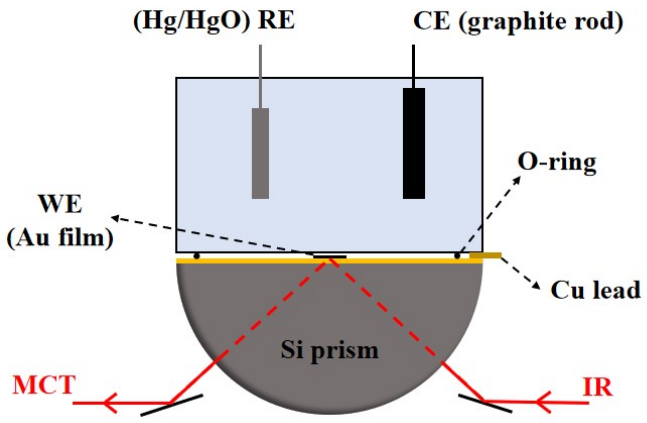

Fig. S1. Schematic illustration of the setup for in situ electrochemical ATR infrared absorption spectroscopy.

The *in situ* electrochemical attenuated total-reflection (ATR) infrared absorption spectral measurement (see Fig. S1) was run on a NQ@FeO_x(OH) active material layer covered on an ca. 60 nm thick Au film chemically deposited on the basal plane of a hemicylindrical Si prism using a Agilent Cary 660 FTIR spectrometer equipped with liquid cooling MCT detector. Then 10 μL above-mentioned catalyst ink was transferred onto an electrochemically polished Au film via a pipette. In this structure, an electrochemical three-electrode system was assembled by using the gold nanometer film as the working electrode (WE) and combining the graphite rod counter electrode (CE) and a Hg/HgO electrode as the reference electrode (RE). In this work, all spectra are expressed in absorbance units defined as $\log(I/I_0)$, where I and I_0 represent the absorption intensities at the sample and reference conditions, respectively.

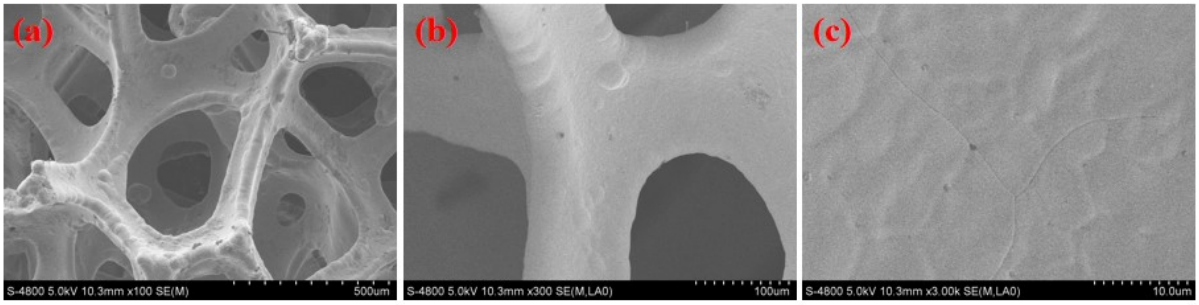

Fig. S2. The SEM images of blank iron foam.

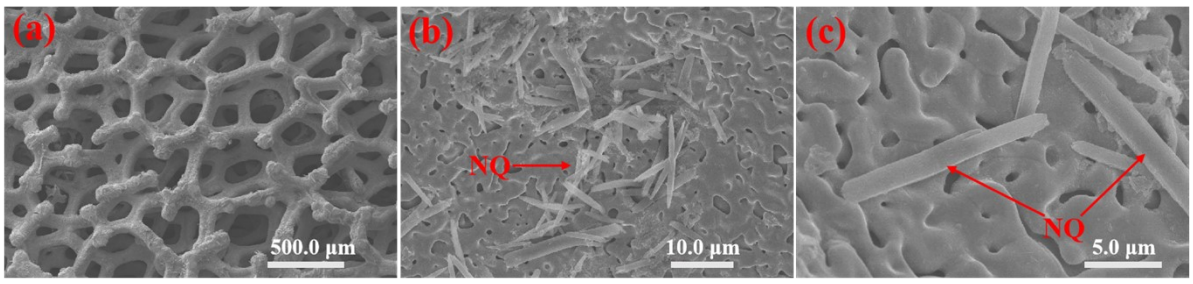

Fig. S3. The SEM images of NQ/IF electrodes

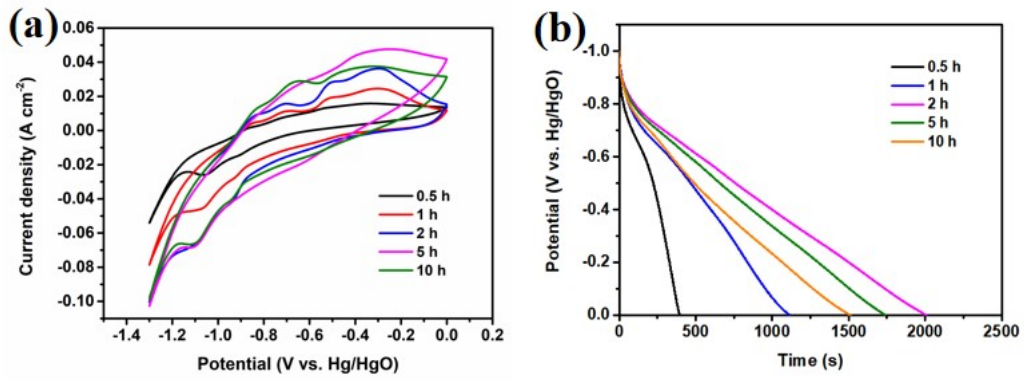

Fig. S4. The electrochemical properties of NQ@FeO_x(OH)/IF electrode produced at different hydrothermal time (0.5 h, 1 h, 2 h, 5 h, and 10 h). (a) CV curves at 10 mV s^{-1}, (b) GCD curves at 4 mA cm^{-2}.

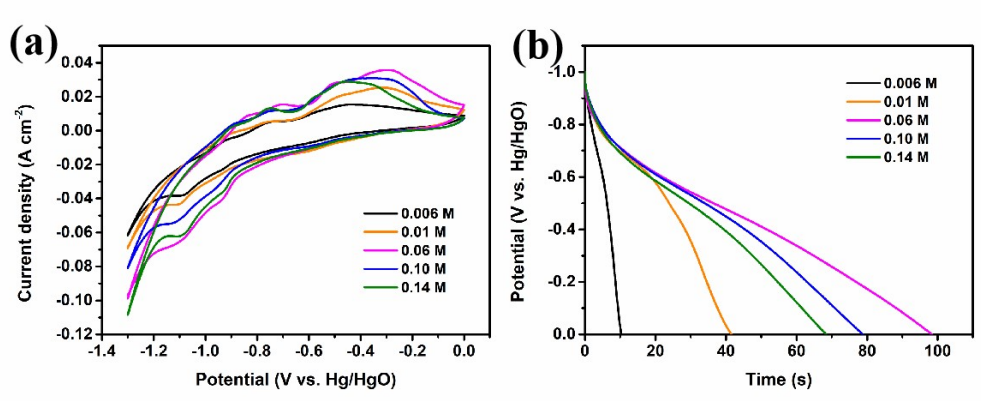

Fig. S5. The electrochemical properties of NQ@FeO_x(OH)/IF electrode synthesised at different concentration of NQ solution. (a) CV curves at 10 mV s^{-1}, (b) GCD curves at 20 mA cm^{-2}.

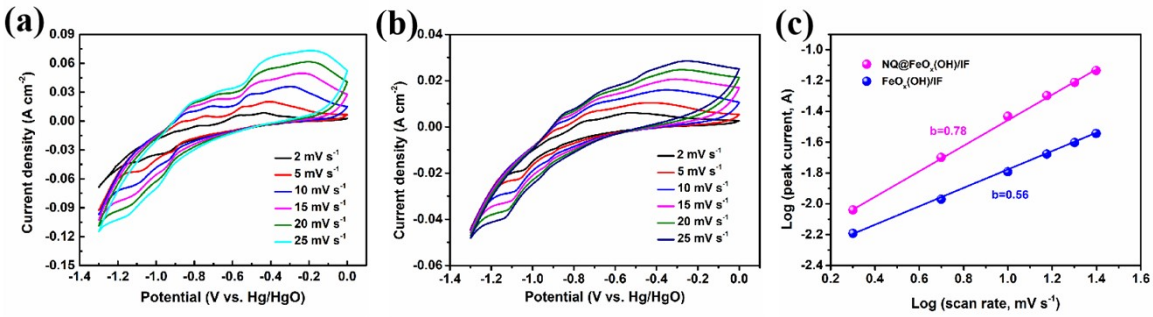

Fig. S6. CV curves of NQ@FeO_x(OH)/IF and FeO_x(OH)/IF (b) at different scan rates from 2 to 25 mV s^{-1}, and (c) the corresponding b-values determined by the linear fitting of cathodic peak currents of CV curves with different scan rates.

Table S1. The comparison of the configuration and specific capacity of various aqueous Fe-based rechargeable batteries.

Anode	Electrolyte	Voltage	Specific capacity	Reference
Fe_3O_4/rGO	8 M KOH + 0.01 M Na_2S	-1.2 ~ -0.4 V	320 mAh g^{-1}	[1]
GE@CNT-Fe-Fe_3C/CF	1 M KOH	-1 ~ 0 V	1.74 mAh cm^{-3}	[2]
C−Fe nanoparticles	1 M KOH	-1.2 ~ 0 V	208 mAh g^{-1}	[3]
3D-Fe/Fe_2O_3@C	1 M KOH	-1.1 ~ 0 V	3.07 mAh cm^{-2}	[4]
Fe_2O_3@GH	6 M KOH	-1.1 ~ -0.2 V	304 mAh g^{-1}	[5]
Fe_3S_4@rGO	6 M KOH + 15 g L^{-1} LiOH	0.6 ~ 1.5 V	343.6 mAh g^{-1}	[6]
Fe_3S_4 microspheres	6 M KOH	0.9 ~ 1.5 V	328.5 mAh g^{-1}	[7]
C@Fe-based/Bi/FF	6 M KOH	-1.1 ~ -0.2 V	2.83 mAh cm^{-2}	[8]
Zn-Fe_2O_3 HPs	1 M KOH	-1.1 ~ 0 V	124 mAh g^{-1}	[9]
Fe_3O_4-NGC	6 M KOH	-1.2 ~ 0 V	308.1 mAh g^{-1}	[10]
Fe_3O_4@C MNAs	2 M KOH	-1.2 ~ -0.2 V	292.4 mAh g^{-1}	[11]
NQ@FeOx(OH)/IF (this work)	6 M KOH	-1 ~ 0 V	2.23 mAh cm^{-2} 348.6 mAh g^{-1}	Present work

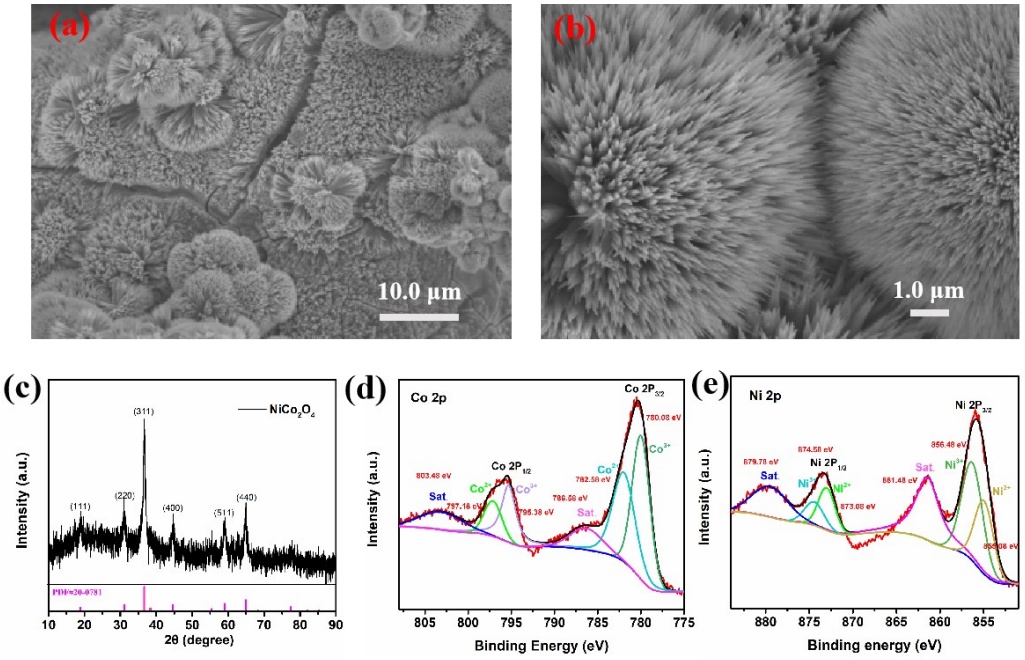

Fig. S7. The SEM (a-b), XRD pattern (c), Co XPS spectrum (d), and Ni 2p XPS spectrum (e) of $NiCo_2O_4$ materials.

$NiCo_2O_4$ was fabricated as cathodic materials using the hydrothermal method, which was proved to be nanowires from the SEM (Fig. S7a-b). Fig. S7c shows the wide-angle X-ray diffraction (XRD) pattern of the $NiCo_2O_4$ nanowires scrapped from $NiCo_2O_4$/NF electrodes. As observed in Fig. S7c, the well-defined diffraction peaks observed at 2θ values of 18.9°, 31.1°, 36.6°, 44.6°, 59.1°, 64.9° and 68.3° could be successfully indexed to (111), (220), (311), (400), (511), and (440) plane reflections of the spinel $NiCo_2O_4$ crystalline structure (JCPDF file no. 20-0781), with the standard peaks indicated by the red lines in Fig. S5c. The X-ray photoelectron spectroscopy (XPS) measurement is further carried out to study the chemical composition of the $NiCo_2O_4$ nanowires, as shown in Fig. S7d-e. The Co 2p spectrum in Fig. S7d can be fitted into both Co^{2+} and Co^{3+} each accompanied with a shakeup satellite, and the Ni 2p spectrum in Fig. S7e can be also best fitted into Ni^{2+} and Ni^{3+} each accompanied with a shakeup satellite. These results indicate that the surface of the $NiCo_2O_4$ nanostructures contains Co^{2+}, Co^{3+}, Ni^{2+}, and Ni^{3+}, which is in good agreement with previous results on $NiCo_2O_4$.

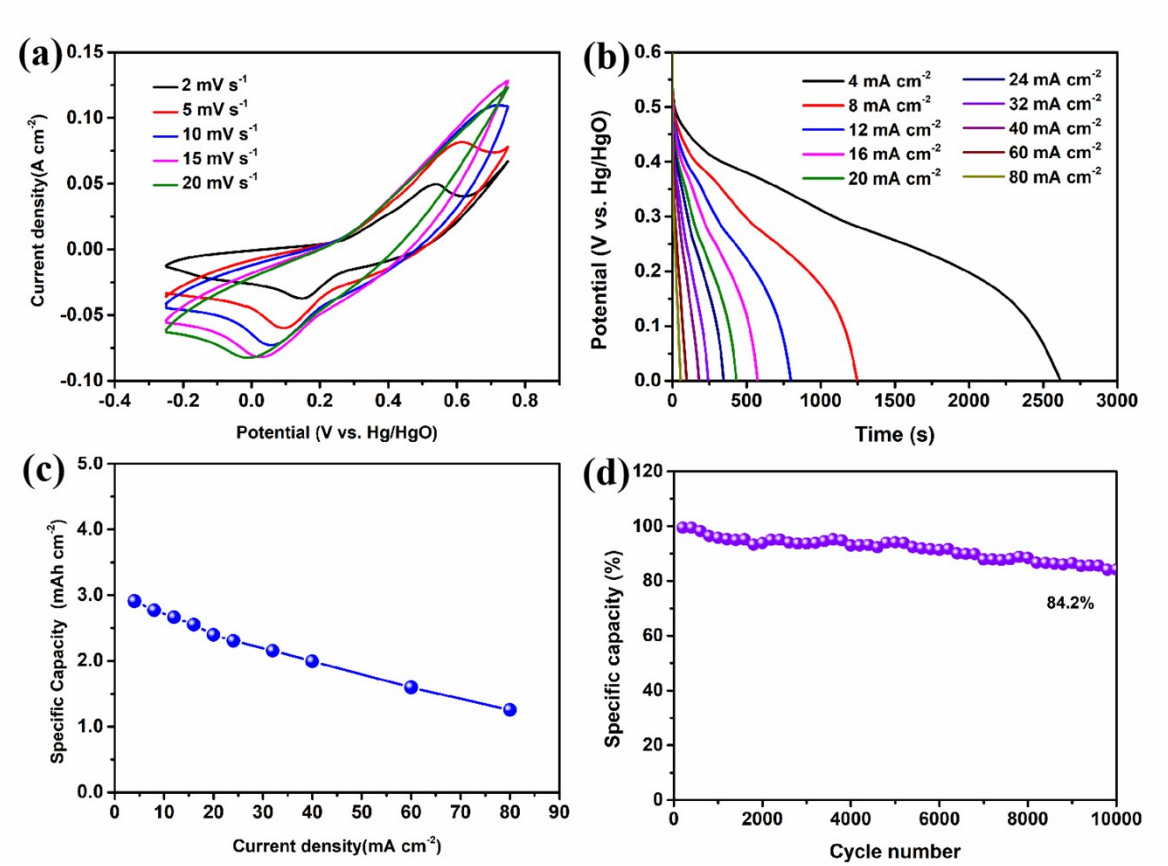

Fig. S8. The electrochemical measurement of $NiCo_2O_4$ cathode. (a) the CV curves at different scan rates from 2 to 20 mV s^{-1}, (b) the GCD curves at different current densities from 4 to 80 mA cm^{-2}, (c) the corresponding specific capacities, (d) the cyclic stability at 60 mA cm^{-2}.

The electrochemical properties of the $NiCo_2O_4$/NF electrode were tested using a three-electrode mode in a 6 M KOH solution. Fig. S8a is the cyclic voltammogram (CV) curves of the $NiCo_2O_4$ nanowire sample. It is found that all the CV curves share a similar shape and the current increases with increasing the scan rates from 2 to 20 mV s^{-1}. A distinct pair of redox peaks is obviously observed, which clearly reveals the pseudocapacitive characteristic of the electrode. The redox peaks can be attributed to the reaction of M–O/M–O–OH (M represents Ni and Co ions) associated with OH^- anions. Also, GCD curves were carried out to study the electrochemical behaviors of $NiCo_2O_4$ cathode at different current densities from 4 to 80 mA cm^{-2} in Fig. S8b. A remarkable calculated areal capacity of 2.9 mAh cm^{-2} is presented at a current density of 4 mA cm^{-2} in Fig. S8c. The cyclic stability was also studied (Fig. S8d). Over 10000 cycles, the $NiCo_2O_4$ electrode exhibits impressive durability (84.2%) at 60 mA cm^{-2}.

Table S2. The comparison of the energy and power density of various aqueous Fe-based rechargeable batteries.

Battery type	Specific capacity	Energy density	Power density	Reference
GE@NiCoO/CF // GE@CNT-Fe-Fe3C/CF battery	1.61 mAh cm^{-3}	1.28 mWh cm^{-3} at 18.32 mW cm^{-3}	18.32 mW cm^{-3}	[2]
$Ni(OH)_2$ MSs@NF //Fe_2O_3@GH battery	127 mAh g^{-1}	203 Wh kg^{-1} at 0.798 kW kg^{-1}	6.4 kW kg^{-1}	[5]
NiO@C//Fe@C battery	138.9 mAh g^{-1}	138 Wh kg^{-1} at 0.61 kW kg^{-1}	14.5 kW kg^{-1}	[12]
Ni-Co DH/OG// Fe_3O_4/FeOOH/OG battery	180 mAh g^{-1}	161.3 Wh kg^{-1} at 5.7 kW kg^{-1}	43 kW kg^{-1}	[13]
Ni@CMFs//Fe@CMFs battery	148.8 mAh g^{-1}	116 Wh kg^{-1} at 5.76 kW kg^{-1}	5.76 kW kg^{-1}	[14]
NiO@C//Fe⊂C cell	160 mAh g^{-1}	140.8 Wh kg^{-1} at 0.65 kW kg^{-1}	15.6 kW kg^{-1}	[15]
P-$NiCo_2O_4$ NWAs// α-Fe_2O_3 NRs battery	134.5 mAh g^{-1}	227 Wh kg^{-1} at 0.59 kW kg^{-1}	23.4 kW kg^{-1}	[16]
NiCoO//rGO/Fe_2O_3 battery	17.6 mAh cm^{-3}	961.6 mWh cm^{-3}	19.9 mW cm^{-3}	[17]
$Ni(OH)_2$/CNT biscrolled yarn//Fe_3O_4/CNT biscrolled yarn battery	0.053 mAh/cm	422 mWh cm^{-3} at 753 mW cm^{-3}	7535 mW/cm^{-3}	[18]
$Ni(OH)_2$@NC/CTs// α-Fe_2O_3@NC/CTs battery	105.6 mAh g^{-1}	155.4 Wh kg^{-1} at 1.75 kW kg^{-1}	14 kW kg^{-1}	[19]
Ni/Fe battery (this work)	1.09 mAh cm^{-2} 147 mAh g^{-1}	235.2 Wh kg^{-1} at 547 W kg^{-1} 19.6 Wh cm^{-3} at 45 W cm^{-3}	5.4 kW kg^{-1} at 82 Wh kg^{-1} 450 W cm^{-3} at 6.8 Wh cm^{-3}	Present work

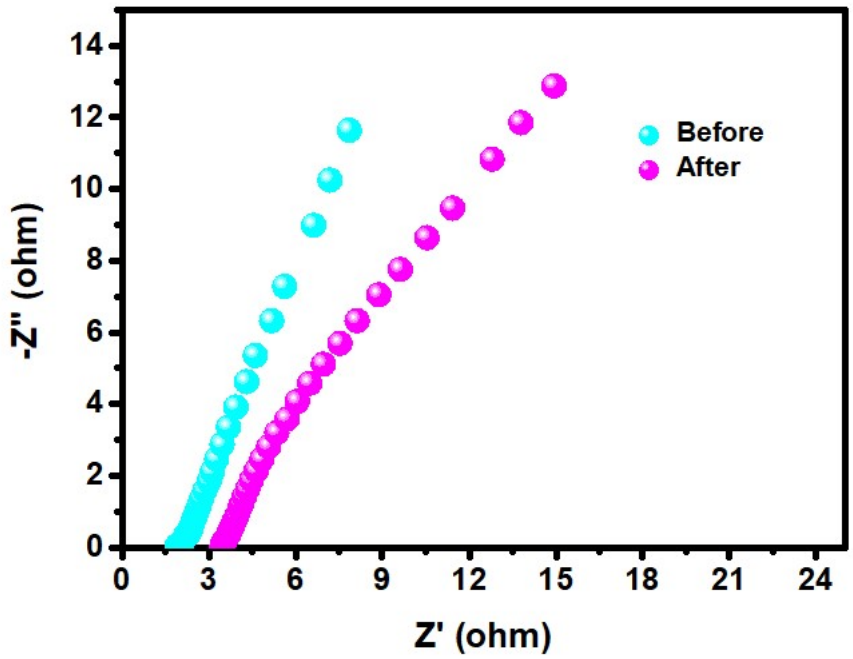

Fig. S9. The Nyquist plots of the 1st and 10,000th cycles for Ni/Fe batteries.

References

1 W. K. Tan, K. Asami, K. Maegawa, R. Kumar, G. Kawamura, H. Muto and A. Matsuda, *Mater. Today Commun.*, 2020, **25**, 101540.

2 X. Li, T. Gao, Q. Liu, Y. Xu, J. Li and D. Xiao, *Mater. Chem. Front.*, 2021, **5**, 3636-3645.

3 X. Wu, H. Zhang, K. J. Huang and Z. Chen, *Nano Lett.*, 2020, **20**, 1700-1706.

4 X. Li, Y. Guo, T. Gao, P. Li, Z. Jin and D. Xiao, *ACS Appl. Mater. Interfaces*, 2021, **13**, 57411-57421.

5 F. Yin, P. Yang, X. Chen, Q. Yang and J. Xie, *Batteries Supercaps*, 2022, **5**, 202100289.

6 C. Wu, J. Zheng, J. Li, T. Jin, F. Wang, Q. Li, M. Chen, J. Qi, S. Gao and E. Shangguan, *J. Alloys Compd.*, 2022, **895**, 162593.

7 J. Li, J. Zheng, C. Wu, H. Zhang, T. Jin, F. Wang, Q. Li and E. Shangguan, *J. Alloys Compd.*, 2021, **874**, 159873.

8 X. Li and D. Xiao, *ChemElectroChem*, 2020, **7**, 3098-3105.

9 H. Shen, B. Lan, C. C. Li, J. Yan, J. Wang, Z. Wang, X. Hu, J. Liu and Y. Wu, *J. Alloys Compd.*, 2021, **879**, 160436.

10 C. Lai, L. Cheng, Y. Sun, K. Lee and B. Lin, *Appl. Surf. Sci.*, 2021, **563**, 150411.

11 T. Zhang, C. Yang, S. Sun, Y. Huang, G. Meng, A. Han and J. Liu, *Sci. China Mater.*, 2021, **64**, 1105-1113.

12 H. Zhang, Y. Liu, T. Meng, L. Ma, J. Zhu, M. Xu, C. M. Li, W. Zhou and J. Jiang, *ACS Sustainable Chem. Eng.*, 2019, **7**, 10995-11003.

13 Z. Qin, Y. Song, H. Y. Shi, C. Li, D. Guo, X. Sun and X. X. Liu, *Chem. Eng. J.*, 2020, **400**, 125874.

14 L. Ma, Y. Xu, Y. Liu, H. Zhang, J. Yao, N. Li, C. M. Li, W. Zhou and J. Jiang, *ACS Sustainable Chem. Eng.*, 2019, **7**, 17919-17928.

15 H. Zhang, L. Li, Y. Liu, T. Meng, L. Ma, M. Xu, J. Zhu, C. M. Li and J. Jiang, *ACS Appl. Mater. Interfaces*, 2019, **11**, 42365-42374.

16 W. Qiu, H. Xiao, W. He, Y. Li and Y. Tong, *Inorg. Chem. Front.*, 2018, **5**, 1805-1815.

17 Y. Guo, C. Chen, Y. Li, Y. Chen, S. Li, T. Gao, H. Liu, W. Liu, D. Xiao and X. Li, *Appl. Surf. Sci.*, 2023, **623**,156995.

18 J. H. Choi, J. Kim, J. H. Noh, G. Lee, C. Yoon, U. C. Kim, I. H. Jang, H. Y. Kim and C. Choi, *Int. J. Mol. Sci.*, 2023, **24**, 1067.

19 W. Li, Q. Xu, D. Kong, H. Yang, T. Xu, H. Wang, J. Zang, S. Huang, X. Li and Y. Wang, *Chem. Eng. J.*, 2023, **452**, 139251.